Electrodeposition of Au–Sn alloys from acid Au(III) baths

B. BOZZINI[1,*], A. FANIGLIULO[1], G. GIOVANNELLI[2], S. NATALI[2] and C. MELE[1]
[1]*INFM – Dipartimento di Ingegneria dell'Innovazione, Università di Lecce, v. Monteroni, I-73100 Lecce, Italy*
[2]*Dipartimento ICMMPM, Università di Roma "La Sapienza", v. Eudossiana 18, I-00185 Roma, Italy*
(*author for correspondence, fax: +39 0832 320525, e-mail: benedetto.bozzini@unile.it)

Abstract

A bath for the electrodeposition of white gold alloys of interest for the electroforming of hollow jewellery is proposed and investigated. The system was an acidic Au(III)–Sn(IV) bath for the electrodeposition of Au–Sn alloys. The electrochemical investigations were based on cyclic voltammetry, linear-sweep voltammetry, galvanostatic electrodeposition experiments and *in situ* Raman spectroscopy. The electrode kinetics of alloy formation were elucidated by stripping voltammetry. The effects of cathodically adsorbed CN^- were studied by *in situ* Raman spectroscopy. Electrodeposited foils were studied from the crystallographic, compositional and morphological points of view. Codeposition of Au and Sn gives rise to a single phase of approximately equiatomic composition over a current density interval of 10 to 40 mA cm^{-2}. This orthorhombic phase is structurally the same as the ζ' phase of the equilibrium Au–Sn system, but its stoichiometry and lattice parameters are different. The equilibrium two-phase δ, ζ' structure can be obtained by heat-treatment.

1. Introduction

The electrodeposition of white precious metals and alloys still requires extensive research and development efforts in order to achieve industrially acceptable quality standards [1, 2]. Alloying effects giving rise to commercially acceptable colours for white Au alloys are not straightforward. The human perception of the colour of metals derives from the following optical properties [3]: (i) spectral reflectivity, broadly related to brightness and (ii) light absorption, broadly related to hue. The former property derives from the mobility of conductance electrons and is related to electrical and thermal conductivity. The latter property depends on the peculiarities of the valence band structure. Alloying changes the colour of Au according to three different mechanisms: (i) modification of the valence band structure, (ii) reduction of the spectral reflectivity, (iii) formation of intermetallic compounds with their own electronic structure. We are currently investigating [4, 5] the electrodeposition of binary and ternary Au alloys with Sn and Zn. This approach is expected to give rise to whitening effects due to all three causes listed above.

The literature on the electrochemical behaviour of the Au–Sn system is very limited [6–8]. Underpotential deposition of Sn on polycrystalline Au and Au(III) has been reported. Two anodic peaks were measured and assigned to the oxidation of Sn° to insoluble oxygenated Sn(II) species and to the oxidation of Sn(II) to soluble

Sn^{4+}. Three patents on high-Au Au–Sn alloys have been filed [9], stressing the bath chemistry, but giving no electrochemical or structural details. Recently a paper providing a sound description of electrodeposition processes from a weakly acidic sulphite bath appeared [10]. Bath preparation is thoroughly described and some morphological data are reported, but limited electrochemical details and no structural data are provided.

In this work an acid Au–Sn bath without free cyanide is formulated and studied. Particular care was devoted to the determination of the crystalline structure.

2. Experimental details

2.1. *Solutions*

A Au(III) bath was used of composition: Au (as KAu(CN)$_4$) 5 g l^{-1}, Sn (as SnCl$_6^{2-}$) 75 g l^{-1}, pH equals 0.5. Analytic grade chemicals were used. The solutions were prepared with ultra-pure water (resistivity 18 MΩ cm) obtained with a Milli-Q system. The Sn complex was prepared by dissolving the metal into aqua-regia. The excess nitrate was eliminated by boiling. The pH was adjusted by adding HCl. The Au(III) salt was dissolved in the Sn(IV) solution. The operating conditions were: current density (c.d.) 10 to 40 mA cm^{-2}, temperature 20 °C.

2.2. Electrochemical experiments

The electrodeposition set-up for the growth of thick layers ($\sim$50 μm) was a revolutioning-cathode cell, described previously [11, 12]. Square-based prismatic Cu cathodes were used: these were of side 1 cm and height 4 cm. A length of 0.75 cm from the top and the bottom of the prismatic cathode were screened with PTFE tape to avoid terminal effects in the c.d. distribution. The substrates were dissolved in concentrated HNO_3 to obtain four foils, separated from the substrate. Uniformity of the average c.d. distribution and fluid flow were ensured by the time-averaging effect of the revolutioning motion of the cathode. The rotation rate was 150 rpm.

Cyclic voltammetry (CV) was carried out in a H cell with electrodic compartments separated by a glass frit. The working electrode was a glassy carbon (GC) disc of diameter 3 mm AMEL model 493. Before each experiment, the GC electrode was cleaned by dipping into aqua regia. The counter electrode was a platinum foil (area 3 cm^2). The reference electrode was Ag/AgCl in all experiments, including spectroelectrochemical ones. The potentials are reported vs Ag/AgCl. The scan rate was 0.04 V s^{-1}, the initial scan direction was from anodic to cathodic.

2.3. Compositional, structural and mechanical investigations

Structural characterisation was performed by X-ray diffraction (XRD), using a Philips PW 1830 diffractometer equipped with a Philips PW 1820 vertical powder goniometer and a Philips 1710 control unit. The scan rate was 1 deg s^{-1}. The radiation was unmonochromated CuK_α. The morphology of the samples was studied using a Cambridge Stereoscan 360 SEM equipped with energy dispersive spectroscopy (EDX) facilities. The composition of the alloys was measured by X-ray fluorescence (XRF, Spectro X-test) and EDX.

The Vickers microhardness was evaluated by the recording hardness measurement (RHM) technique with a Fischerscope H100. The loading sequence consisted in applying a loading ramp reaching 200 mN in 30 s and holding at the maximum load for 10 s. Data from loading and unloading curves were treated as illustrated in [13]. Average data and 95% confidence intervals were estimated from five independent measurements.

2.4. Quantification of colour

Measurements of alloy colour were carried out by evaluating the CieLab coordinates with a X-Rite SP62 colorimeter. The CieLab coordinates L, a and b are claimed to quantify the human perception of the factors affecting the perception of colour: 'hue' H (the colour proper, in terms of spectral adsorption of visible light), 'lightness' L (i.e. brightness) and 'chromaticity' C (i.e., the distance from the pure hue). L directly quantifies the lightness, a is the red/green axis, b is the yellow/blue

axis. The values of a and b define the hue H, while the chromaticity C is defined as $C = (a^2 + b^2)^{1/2}$.

2.5. In situ surface-enhanced Raman spectroscopy (SERS)

SERS measurements were carried out with a true confocal Raman microprobe system (LabRam Jobin-Yvon) with excitation at 632.8 nm provided by a He–Ne laser. The power delivered to the sample was 12 mW. A 10× long-working-distance objective was used. In situ electrochemical measurements were performed in a Ventacon cell with a vertical polycrystalline Au disc working electrode 3 mm in diameter embedded into a Teflon holder. The counter electrode was a Pt wire. Normalisation of the spectra was performed by dividing them by the peak value after background subtraction.

3. Results and discussion

3.1. Cyclic voltammetry

Calibration CV experiments were run in the supporting electrolyte (Figure 1A) and in the Au(III) solution (Figure 1B). Figure 1B shows the first scan, measured with a clean GC electrode; a nucleation loop is seen. Subsequent scans, not reported for brevity, show that Au can be deposited at potentials less cathodic than the values required for hydrogen evolution with a clean GC. After a given surface coverage with Au nuclei is attained, hydrogen evolution occurs along with Au electrodeposition. The absence of nucleation features and the serration in the cathodic c.d. plots in subsequent scans support this interpretation. No anodic features are observed in the potential range investigated.

The features of the voltammetric behaviour of the Au–Sn alloy depend on the cathodic terminal voltage and can be assigned to two classes, typified by Figures 2 and 3. The cathodic going scan for the same solution without Sn(IV) is shown in Figure 3, for comparison.
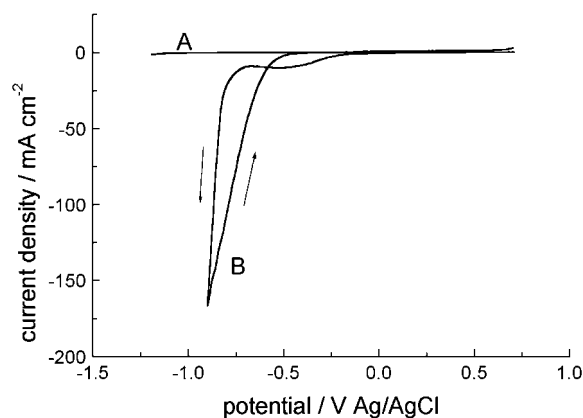

Fig. 1. Cyclic voltammograms of a glassy carbon electrode in HCl solution of pH 0.5 without (A) and with (B) 5 g l^{-1} of Au(III). Scan rate 40 mV s^{-1}.
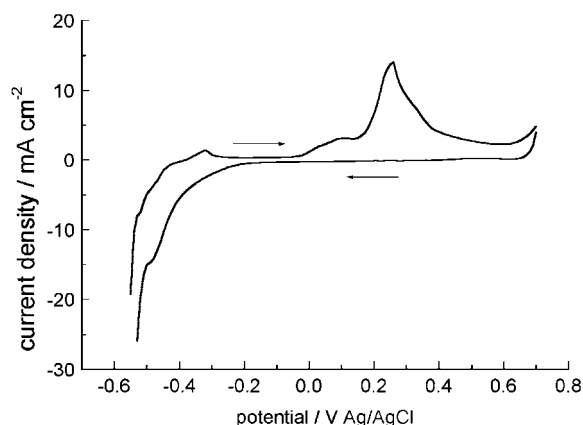
Fig. 2. Cyclic voltammograms of a glassy carbon in the Au(III)–Sn(IV) bath. Cathodic terminal potential −0.6 V vs Ag/AgCl. Scan rate 40 mV s^{-1}.
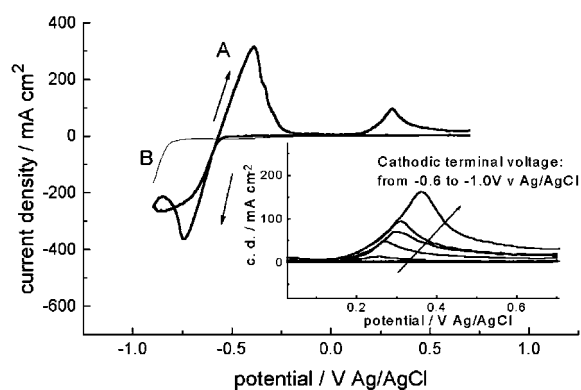

Fig. 3. Cyclic voltammograms of a glassy carbon in the Au(III)–Sn(IV) bath (A). Cathodic terminal potential −0.9 V vs Ag/AgCl. Scan rate 40 mV s^{-1}. The behaviour of the Au(III) bath is also shown (B), for comparison. Inset: the behaviour of the nobler anodic peak as a function of the cathodic terminal potential.

The cathodic branch of these voltammograms displays a Tafel growth (Figure 2) followed by a maximum (Figure 3). The anodic branch shows one peak around +0.3 V if the cathodic terminal voltage does not exceed −0.6 V (Figure 2). A second anodic peak appears for more cathodic polarization values (Figure 3). Of course, the details of peak potential and c.d. depend on the scan rate and number of scan repetitions. A more detailed discussion of this topic is beyond the scope of this paper, which is mainly intended as a report of the salient qualitative features of the electrochemical behaviour of this alloy-electrodeposition system.

The nobler anodic peak cannot be attributed to gold, which has been shown not to oxidize in this potential range in the relevant environment (Figures 1 and 3B) and can be explained with alloy formation. The anodic behaviour giving rise to this peak is not affected by changing the cathodic terminal voltage (Figure 3, inset). In fact, the peak starts at the same potential irrespective of the cathodic terminal potential and the peak position and area depend on the amount of material deposited in the cathodic going scan, which is positively correlated

with the cathodic terminal potential. This suggests that one well defined phase is grown. The less noble anodic peak is not well defined in terms of electrode potential and tends to shift cathodically as the cathodic terminal potential is increased. This behaviour is typical for an active corrosion process and can be related to the acidic attack of a second phase, possibly Sn, deposited separately after the limiting current density for the alloy deposition has been attained. The initial cathodic c.d. rise in Figures 2 and 3 can thus be attributed to the codeposition of an Au–Sn alloy. The maximum can be explained with mass-transport controlled alloy deposition and the eventual cathodic c.d. growth can be related to the hydrogen evolution reaction.

3.2. In situ SERS experiments

In situ vibrational spectroscopy measurements during the electrochemical growth of an alloy have not been reported in the literature, to the best of the authors knowledge. No previous reports on in situ SERS work on KAu(CN)$_4$ are known to the authors. Spectroelectrochemistry of the ligands is expected to disclose alloy-related peculiarities, in terms of lateral interactions and fractional coverage.

We carried out comparative SERS work on the v(CN) band in the Au(III) bath, without and with the addition of Sn(IV), in the alloy-deposition potential range. Figures 4 and 5 display potential-dependent spectra from the Au and Au–Sn baths. Many kinds of v(CN) bands have been observed during the electrodeposition of Au from Au(CN)$_2^-$ [14]. In the present case, all the reported spectra, with one exception, display a band containing only one dominating contribution due to adsorbed CN$^-$ onto Au. The CN band in the spectrum at −0.3 V in Figure 4 contains contributions from two different states. By multiple gaussian fitting, the peak has been resolved into two contributions: one in the range 2102–2118 cm^{-1}, corresponding to surface CN$^-$ and one at 2158 cm^{-1}, corresponding to Au(CN)$_4^-$. This band assignment has been further supported by FTIR measurements of the Au(CN)$_4^-$ solution.

Fig. 4. In situ Raman spectra of the v(CN) stretching vibration as a function of electrode potential in a deposition bath containing Au(III).
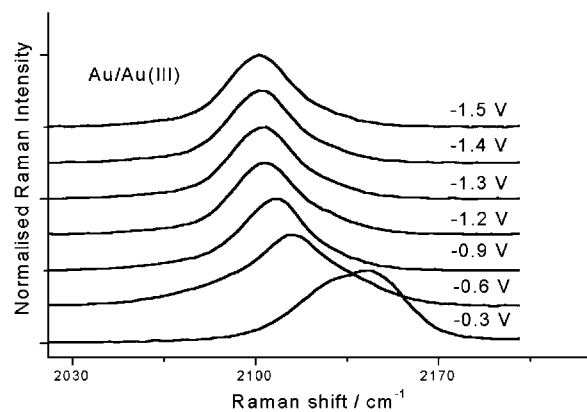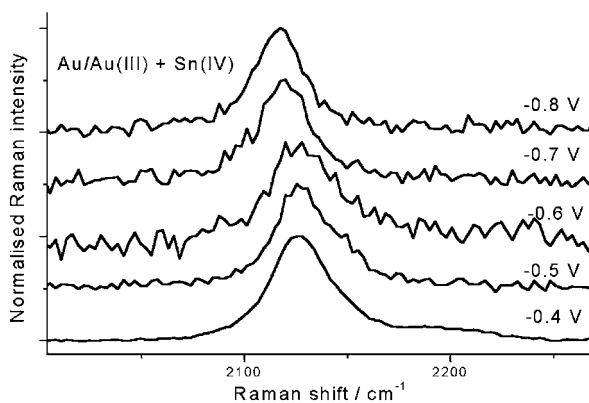
Fig. 5. *In situ* Raman spectra of the ν(CN) stretching vibration as a function of electrode potential in a deposition bath containing Au(III) and Sn(IV).

It is known that bands relating to surface species can undergo potential-dependent shifts of the peak position (Stark-tuning). Several theoretical treatments can be found in the literature of the electrochemical Stark-tuning of the stretching frequencies of CO [15–18], CN [19] and metal–carbon [20] for adsorption onto a range of electrode materials and crystal orientations. The field has been recently reviewed [21, 22]. Classical and quantum mechanical treatments of this phenomenon have been proposed. Different physical factors possibly giving rise to the Stark-tuning have been stressed. Notwithstanding the comparatively considerable effort devoted to this topic, no conclusive treatments appear to have been published. Even though it is not straightforward to summarise and separate the different kinds of contribution to the Stark-tuning considered by the different authors, mainly owing to the different kinds of approach adopted in specific papers, it is nevertheless possible to identify three main kinds of effect. The boundaries between these effects are not absolutely clear-cut and one can argue that these concepts overlap to some extent. With this note of caution in mind, we propose the following tentative list of effects: (i) molecular, (ii) local electric field and (iii) geometric. In the authors' opinion, the single papers which highlight there individual factors most clearly are [15], and [17], respectively [16] accounts for the transition between the ground state of the nuclear hamiltonian to the first vibrationally excited state of the molecule, occurring in such a way that all nearby adsorbates vibrate in-phase. The adopted hamiltonian exhibits the following properties: (i) neglects depolarization and damping, (ii) includes dipole–dipole coupling, (iii) includes variations of charge density with the applied potential and (iv) includes effects of adsorbate coverage. [15] treats a single molecule adsorbed onto a cluster of 14 Pt atoms. Lowest-order harmonic oscillations are taken into account. The bonds are described by pairwise Morse (C–O, Pt–O) and Lennard–Jones (Pt–C) potentials. First and second-order terms are retained in the expansion of the force constants. A direct linear dependence of

the metal-molecule binding energy on the applied electrochemical potential was assumed and treated perturbatively. [17] considers the differences in the Stark-tuning induced by adsorption onto edge and terrace sites. All explanations based on dipolar absorbate-field interactions have been shown to fail to account for the observed effects. Since at a metal surface the electric field varies strongly over atomic dimensions, the field gradient can be so large that its interaction with the molecular quadrupole moment is comparable to the dipolar interaction. The Stark-tuning would thus yield information on atomic-scale features of the electrode.

The molecular factor is thus related to the electronic structure of the adsorbed molecule and is affected by the nature of the bonding to the electrode via donation and back-donation terms. The local electric field factor is linked to the environment of the relevant adsorbate, such as degree of coverage or coadsorption of different molecules. The geometric effect depends on the peculiar morphological feature to which the relevant molecule is adsorbed.

The results of the explanations put forward in the above-mentioned papers can be summarized with the following formula for the peak position of the CN stretching band:

$$\nu(V) = \nu_{\mathrm{fm}} - C \cdot E_{\mathrm{B}}(\mathrm{M–X}) + (A_{\mathrm{m}} + A_{\mathrm{lf}} + A_{\mathrm{g}}) \cdot V \quad (1)$$

where V is the electrode potential, ν_{fm} is the peak position for the free molecule, C is a positive constant, $E_{\mathrm{B}}(\mathrm{M–X})$ is the metal (M)–adsorbate (X) binding-energy and A_{m}, A_{lf} and A_{g} are the molecular, local field and geometric contributions to the Stark-tuning, respectively. According to this approach the Stark-tuning rate is expressed as the sum of three separately linear contributions: $\mathrm{d}\nu/\mathrm{d}V = (A_{\mathrm{m}} + A_{\mathrm{lf}} + A_{\mathrm{g}})$. It is not obvious to separate these effects and specific experiments might be designed. Metal-electrodeposition processes provide a rich dynamic scenario which can afford some form of ranking among these factors. In particular, differences in Stark-tuning rates $\Delta_{12}(\mathrm{d}\nu/\mathrm{d}V) = A_{\mathrm{m1}} - A_{\mathrm{m2}} + A_{\mathrm{lf1}} - A_{\mathrm{lf2}} + A_{\mathrm{g1}} - A_{\mathrm{g2}}$ obtained in correspondence of different plating conditions 1 and 2 can provide useful information. If plating takes place from a single cyanocomplex, such as $\mathrm{Au(CN)_4^-}$, the only known form of Au(III) cyanocomplex, molecular factors are expected to be affected to a minor extent by plating conditions and consequently: $A_{\mathrm{m1}} - A_{\mathrm{m2}} \ll A_{\mathrm{lf1}} - A_{\mathrm{lf2}}$, $A_{\mathrm{g1}} - A_{\mathrm{g2}}$. Since the plating rate is a function of the cathode potential and the morphology of the electrodeposit depends on the plating rate, in general it is expected that the geometrical factor is a function of the potential $A_{\mathrm{g}}(V)$. If this is the case, and if the spectroscopic signal derives from adsorbates bound to geometric features which are specific of the growth conditions, a nonlinearity of the Stark-tuning rate is expected. Of course with SERS the enhancing morphological features might be invariant with the growth rate (e.g., adatoms) and nonlinearity might not be observed even in the presence of major

morphological evolutions of the cathode surface taking place as a function of applied potential or time. Nonlinearity in the Stark-tuning might derive from surface coverage effects: in the case of electrochemical systems without a faradic reaction, these have been found to be notable close to the PZC [23]. In the case of metal-plating systems, it can be assumed that full monolayer coverage is attained as soon as the metal-plating reaction sets in. The use of additives can give rise to coadsorption effects, which can cause the quantity $A_{lf1} - A_{lf2}$ to be sizeable. In addition, local variations of the cathode composition might give rise to local-field variations with respect to a reference composition. Inhomogeneous surface alloying or partial coverage with underpotentially deposited layers are therefore expected to bring about variations of this quantity.

We can thus make use of the potential-dependence of the v(CN) band as a diagnostic of phenomena occurring during the metal plating process in terms of the following effects. (i) Deviations from linearity of the Stark-tuning rate can be related to geometrical variations of the adsorption sites $dv/dV \propto A_g(V)$. (ii) Differences in the Stark-tuning rate between an additive-free bath 1 and a bath 2 containing an additive $\Delta_{12}(dv/dV) \simeq (A_{lf1} - A_{lf2})$ can account for differences in the chemical environment of the adsorbed CN⁻. (iii) Variations of the intercept of the linearized peak position v potential curve can give direct information on changes in the binding-energy of the adsorbate to the cathode: this information can be useful in the case of alloy electrodeposition processes or of electroplating in the presence of metal ions giving rise to underpotential deposition. Molecular level information can thus be derived, relevant to the cathode conditions during the metal electrodeposition process.

We analysed the potential dependence of the peak position for the Au(III) and Au(III)–Sn(IV) baths (Figures 4 and 5, respectively). Owing to the reduction of the enhancing effect due to the codeposition of Sn, the potential range over which the alloy system can be analysed is restricted. Nevertheless potentiostatic alloy formation (Au ~75%) in this potential range has been proved by EDX. The potential-dependent peak positions and respective 95% confidence intervals are reported in Figure 6. A typical example of the gaussian fit of a peak is shown in the inset. The potential-dependence is slightly nonlinear for both systems, with a dominance of the Au(III) bath. As commented above, this effect might be related to both geometrical and compositional causes (potential-dependent alloying, A_{lf}). Since we proved by XRF and EDX that the alloy composition exhibits a negligible variation within the potential range investigated, it is possible to explain the observed nonlinearity as mainly due to geometrical factors (A_g). This nonlinearity implies a decrease of the Stark-tuning rate as the potential grows cathodic. This kind of behaviour can be interpreted in terms of the results reported in [17] as an increasing contribution of edge v terrace adsorption sites. Of course in a metal
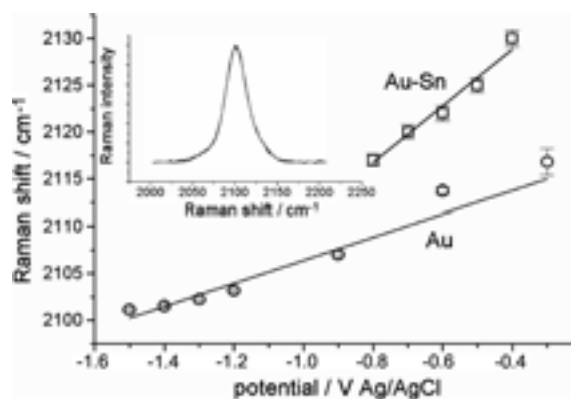

Fig. 6. Peak position of the v(CN) stretching band as a function of the applied electrode potential in the Au(III) and Au(III)–Sn(IV) baths. 95% confidence intervals for the peak positions are reported. Inset: a typical (−1.5 V vs Ag/AgCl, Au(III) bath) v(CN) band and the respective gaussian fit.

plating system the dynamic surface morphology gives rise to a definitely more complex scenario than the static high-index single crystal case dealt with in [17]. Nevertheless relatively higher vibrational frequencies seem to correlate with a higher surface density of protruding features possibly of atomic dimensions. In accord with SEM surface micrographic observations (Figure 7), this behaviour might relate to unstable growth.

If the slightly nonlinear potential dependence is interpolated linearly (Figure 6), different slopes are obtained for Au and Au–Sn: 14 ± 0.7 and 31 ± 3 cm⁻¹ V⁻¹, respectively. A similar behaviour has been observed by *in situ* FTIR in the case of Cd and Cu UPD monolayers on Au [24] and is compatible with the metal effects recently studied by DFT for CO adsorption [18]. This difference in Stark-tuning rates can be interpreted within the simple theoretical framework set up with Equation 1 as a molecular effect giving rise to a modification of the 5σ donation and $2\pi^*$ back-donation terms. The higher Stark-tuning rate of the alloy system can be understood as due to increased back-donation from less noble metals [18]. The different absolute values of the peak positions at a given potential between the Au and the alloy systems can be interpreted in terms of different binding-energies of CN⁻ to the metal substrate: a lower binding energy is predicted for the Au–Sn alloy with respect to Au.

Owing to the progressive loss of SE effect (Figures 4 and 5), it was impossible to record well-resolved spectra at potentials lower than −0.8 V, where codeposition of the Sn-rich, readily oxidized phase is observed. A specific experiment on this effect was devised. Freshly polished Au surfaces were polarized at a potential within the alloy deposition range (−0.4, −0.5 and −0.6 V) and spectra were recorded as a function of time. A progressive reduction of both v(CN) band intensity and background was observed. The SERS background is in fact known to derive from the same surface-enhancing effects affecting the vibrational bands [25]. The analysis of these transients can yield information on the rate of
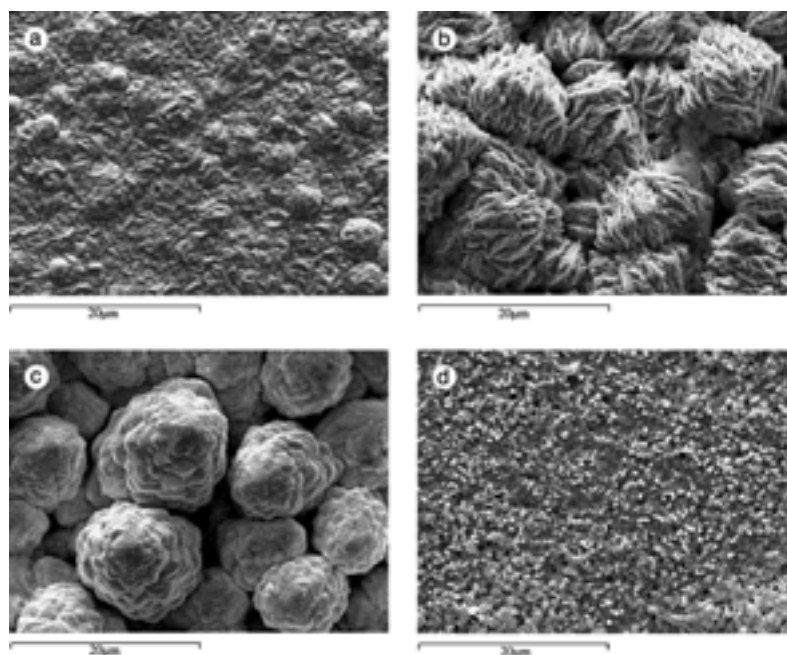
Fig. 7. Scanning electron micrographs of Au–Sn electrodeposits obtained at the following current densities: (A) 10 mA cm^{-2}, as-plated; (B) 20 mA cm^{-2}, as-plated; (C) 40 mA cm^{-2}, as-plated; (D) 10 mA cm^{-2}, heat-treated at 180 °C for 2 h.

surface coverage of the originally SERS-active elements with inactive alloy elements. The fact that a single alloy phase of approximately constant composition forms in a wide range of electrochemical conditions, suggests the use of this alloy-plating process as a model system. The SERS intensity I_{SERS} is directly proportional to the surface concentration of SERS active elements Γ. The loss of SE activity can be modelled as a time and potential-dependent surface coverage of SERS active elements with the inactive material $\theta_a(t,V)$. $I_{SERS}(t,V)$ transients can thus be used to evaluate quantities related to the nucleation of the alloy onto a given initially SERS active substrate, characterized by a known value of Γ (Equation 2).

$$I_{SERS}(t,V) \propto \Gamma \cdot \theta_a(t,V) \qquad (2)$$

In the present case the experimental transients of both the $v(CN)$ band intensity and the background at 1800 cm^{-1} were empirically modelled by an exponential decay with time constant τ (Table 1). The peak and background time constants match reasonably and support the view of the loss of SERS enhancement. The values of τ are anticorrelated with the cathode potential and consequently with the growth rate.

3.3. Properties of galvanostatically electrodeposited layers

Electrodeposition was performed galvanostatically at 10, 20 and 40 mA cm^{-2}. The thickness of the films was about 50 μm. The following properties of electrodeposited layers were investigated: (i) composition and current efficiency, (ii) colour, (iii) morphology. Limited compositional variations around 75% Au (1/3 atomic ratio) were noticed (Table 2). Cathodic efficiency values are also reported in Table 2.

The decolouring effects were assessed by CieLab measurements (Table 3). The results of electrodeposited samples were compared with standard metallurgical white-Au alloys (Au–Ni, Au–Pd) and electrodeposited Rh. The effect of c.d. on colour is hardly observable. The electrodeposited Au–Sn alloys show excellent hue and spectral reflectivity values.

The morphology of the deposits is smooth for the layers plated at lower c.d.s and it tends to grow unstable for higher electrodeposition c.d.s, with formation of globular structures (Figure 7A, B, C). The strongly

Table 1. Time constants τ (Equation 2) for the decay of the Raman intensity at the peak of the $v(CN)$ band I_{CN} and at the background measured at 1800 cm^{-1} I_B during potentiostatic electrodeposition experiments

Electrodeposition potential /V	$\tau(I_{CN})$ /s	$\tau(I_B)$ /s
−0.4	575	493
−0.5	176	205
−0.6	74	108

Table 2. Composition and cathodic efficiency for galvanostatically deposited Au–Sn alloys

Current density /mA cm^{-2}	Average Au content /% ± 1 standard deviation	Cathodic efficiency /% ± 1 standard deviation
10	78.2 ± 1.5	82.1 ± 2.4
20	75.3 ± 1.9	76.4 ± 2.6
40	73.2 ± 0.9	71.1 ± 4.3

Table 3. CieLab colour parameters for white precious metal systems: electrodeposited Au–Sn, metallurgical Au–Ni (Au 75%, Cu 15.5%, Ni 55%), metallurgical Au–Pd (Au 75%, Ag 11%, Cu 3%, Ni 6%, Pd 5%), electrodeposited Rh

White precious metal	L	a	b
Au–Sn electrodeposited	82.352	1.006	14.825
Au–Ni metallurgical	82.802	3.103	14.972
Au–Pd metallurgical	80.874	2.257	15.694
Rh electrodeposited	86.575	2.000	15.875

complexed Au(III) species tend to yield smooth layers while higher growth rates, achieved with simultaneous hydrogen evolution, are correlated with unstable growth front evolution. Heat treatment brings about smoothing of the surface morphology, which might relate to the crystalline phase change (Figure 7D).

3.4. *Crystallographic structure*

As-plated Au–Sn samples of composition about 75% Au, obtained by electrodepositing in the c.d. range 10 to 40 mA cm^{-2}, show a structure whose diffraction peaks sequence is the same as for the orthorhombic ζ'-Au$_5$Sn (Figure 8). These single-phase deposits display a hardness of $157 \pm 32\ HV_{25}$. After heat treatment at 180 °C for 2 h under Ar atmosphere the δ-AuSn structure forms (the equilibrium structure at room temperature for this composition is two-phase ζ', δ) (Figure 8). The superlattice structures for the ordered ζ' phase observed by [26] could not be detected in this work. After heat-treatment, in addition to the growth of the peaks of the δ phase and a decrease of those of the ζ'-type one, lattice parameters of the latter structure are shifted by about 0.27% towards lower lattice spacing. These facts can be interpreted in the following way: a metastable ζ'-type structure is obtained by electrodeposition in the as-plated conditions with stoichiometry Au/Sn=3/1, induced by the electrodeposition process, different from the equilibrium one (Au/Sn=5/1). Heat treatment brings about an evolution of this structure towards the two-
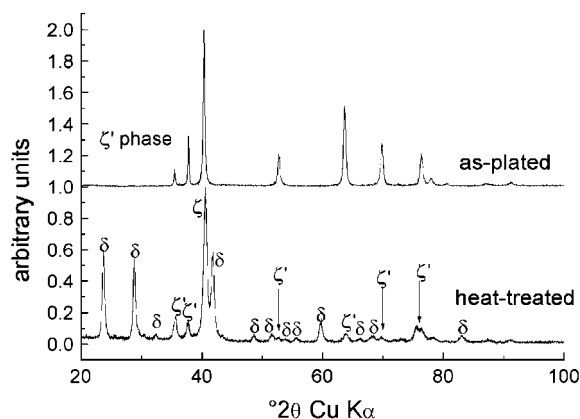
phase equilibrium system. The diffractograms of the ζ' phase resulting from heat-treatment are shifted towards a shrunk structure, which is compatible with a stoichiometry richer in Au (which has a smaller atomic dimension by about 9.7%).

3.5. *Correlations among electrochemical, structural and compositional results*

The CV results exhibit a single stripping peak for cathodic potentials lower than a threshold value, after which a readily oxidized species, probably Sn, is formed concomitantly. This electrochemical information suggests that a single alloy phase is produced for a rather wide range of cathodic polarisation values. The SERS results show a behaviour of the Stark tuning which is consistent with the adsorption of CN$^-$ onto a single SERS active metallic surface whose charge-transfer behaviour (enhanced back-donation) with respect to the adsorbate is typical for less noble metals than Au. The differences in the intercepts of the linear Stark tuning model between Au and the alloy suggest that the binding energy of adsorbed CN$^-$ is lower in the case of the alloy, this fact might in part account for the depolarizing action of Sn(IV) in the electroplating bath. The crystallographic results prove that the Au–Sn alloys grown in a range of electrochemical conditions are indeed the same, single phase. The compositional analyses show that the stoichiometry of these alloys is reasonably constant in the same range of electrodeposition conditions. The colour analyses confirm the fact that the alloys electrodeposited in this work exhibit sizeably the same interaction with visible light.

4. Conclusions

In the acid Au(III)–Sn(IV) system studied in this work the codeposition of the alloying elements gives rise to the formation of a single phase with a limited compositional range, as shown by X-ray diffractometry and by anodic stripping voltammetry. The Au–Sn phase obtained by electrodeposition is metastable and can be transformed into the equilibrium two-phase system by heat treatment. SERS investigations of the cathodically adsorbed CN$^-$ have revealed the effects of the codeposition of Sn with Au, in terms of variations of the interaction of the adsorbate with the growing metal film. These adsorption effects can be related to the depolarizing action of Sn observed by electrochemical methods. Electroformed objects of white Au alloys with good chromatic properties can be prepared with the proposed acid bath. This material is of perspective interest for the electroforming of 75% Au white hollow jewellery.

Fig. 8. X-ray diffractograms of about 75% Au Au–Sn electrodeposit obtained at 40 mA cm^{-2}. As-plated (non-stoichiometric ζ' phase) and heat-treated (180 °C, 2 h, Ar atmosphere; δ and stoichiometric ζ' phases).

References

1. B. Bozzini and P.L. Cavallotti, *Trans. IMF* **78** (2000) 227.
2. P. Bagnoud, S. Nicoud and P. Ramoni, *Gold Technology* **18** (1996) 11.

754

3. B. Bozzini, *AIFM Galvanotecnica e Nuove Finiture* **3** (1993) 199.

4. B. Bozzini, P.L. Cavallotti, G. Giovannelli and S. Natali, Elettrocristallizzazione di leghe binarie Au–Sn a composizione stechiometrica, XX Congresso Nazionale della Società Chimica Italiana, Rimini, 4–9 giugno, 2000, EL-OR003.

5. B. Bozzini, P.L. Cavallotti, G. Giovannelli and S. Natali, 'Electrodeposition And Structural Characterisation Of Au–Sn Alloys', Proceedings of the 15th World INTERFINISH Congress, 13–15 Sept. (2000), Garmisch-Partenkirchen, Germany.

6. V.A. Vicente and S. Bruckenstein, *Anal. Chem.* **44** (1972) 297.

7. A. Rodes, J.M. Feliu, A. Aldaz and J. Clavilier, *J. Electroanal. Chem.* **256** (1988) 455.

8. A. Rodes, E. Herrero, J.M. Feliu and A. Aldaz, *J. Chem. Soc., Faraday Trans.* **92** (1996) 3769.

9. W. Zilske, Electrolytic bath and process for the deposition of gold alloy coatings, US Patent 4 391 679; P. Stevens, Tin–gold electroplating bath and process, US Patent 4 013 523; F. Zantini, Electrodeposition of gold alloys, US Patent 3 764 489.

10. W. Sun and D.G. Ivey, *Mat. Sci. Eng.* **B65** (1999) 111.

11. B. Bozzini, G. Giovannelli and P.L. Cavallotti, *J. Appl. Electrochem.* **29** (1999) 685.

12. B. Bozzini, G. Giovannelli and P.L. Cavallotti, *J. Appl. Electrochem.* **30** (2000) 591.

13. F.R. Brotzen. *Intern. Mat. Rev.* **39** (1994) 24.

14. B. Bozzini and A. Fanigliulo, *J. Appl. Electrochem*, in press.

15. C. Korzeiewski, S. Pons, P.P. Schmidt and M.W. Severson, *J. Chem. Phys.* **85** (1986) 4153.

16. D.K. Lambert, *J. Chem. Phys.* **89** (1988) 3847.

17. J.S. Luo, R.G. Tobin, D.K. Lambert, G.B. Fisher and C.L. DiMaggio, *J. Chem. Phys.* **99** (1993) 1347.

18. S.A. Wasileski and M.J. Weaver, *Faraday Discuss.* **121** (2002) 285.

19. K. Ashley, F. Weinert and D.L. Feldheim, *Electrochim. Acta* **36** (1991) 1863.

20. S. Zou and M.J. Weaver, *J. Phys. Chem.* **100** (1996) 4237.

21. D.K. Lambert, *Electrochim. Acta* **41** (1996) 623.

22. T. Iwasita and F.C. Nart, *in* H. Gerischer and C.W. Tobias (Eds), 'Advances in Electrochemical Science and Engineering' (VCH, Weinheim, 1995), p. 123.

23. A.B. Anderson, R. Kötz and E. Yeager, *Chem. Phys. Lett.* **82** (1981) 130.

24. B. Bozzini, *Faraday Discuss.* **121** (2002) 231, 345.

25. C.Y. Chen, E. Burstein and S. Lundquist, *Solid State Comm.* **32** (1979) 63.

26. K. Osada, S. Yamaguchi and M. Hirabayashi, *Trans. Jpn. Inst. Met.* **15** (1974) 256.